

Nonlinear Electrokinetic Transport Under Combined ac and dc Fields in Micro/Nanofluidic Interface Devices

Vishal V. R. Nandigana

e-mail: nandiga1@illinois.edu

N. R. Aluru¹

e-mail: aluru@illinois.edu

Department of Mechanical
Science and Engineering,
Beckman Institute for Advanced
Science and Technology,
University of Illinois at Urbana-Champaign,
Urbana, IL 61801

The integration of micro/nanofluidic devices led to many interesting phenomena and one of the most important and complex phenomenon among them is concentration polarization. In this paper, we report new physical insights in micro/nanofluidic interface devices on the application of ac and dc electric fields. By performing detailed numerical simulations based on the coupled Poisson, Nernst-Planck, and incompressible Navier-Stokes equations, we discuss electrokinetic transport and other hydrodynamic effects under the application of combined ac and dc electric fields for different nondimensional electrical double layer (EDL) thicknesses and nanochannel wall surface charge densities. We show that for a highly ion-selective nanochannel, the application of the combined ac/dc electric field, at amplitudes greater than the dc voltage and at a low Strouhal number, results in large dual concentration polarization regions (with unequal lengths) at both the micro/nanofluidic interfaces due to large and unequal voltage drops at these junctions. The highly nonlinear potential distribution gives rise to an electric field and body force that changes the electrokinetic fluid velocity from that obtained on the application of only a dc source. [DOI: 10.1115/1.4023442]

Keywords: micro-nanofluidic channel, concentration polarization, induced space charge, ac/dc field, electrokinetic transport

1 Introduction

The advent of lab-on-a-chip devices has led to many developments in the areas of biological sensing, mixing, drug delivery, etc. [1–4]. The application of external electric fields to drive the fluids inside such devices aids in better control when compared to using pressure driven techniques. The fluid is transported through electroosmosis, which refers to the bulk motion of a fluid containing charged species under the action of an applied electric field [5]. Electroosmotic fluid transport has found applications in membrane separation, cell trapping processes, etc. [6,7]. The transport phenomenon inside nanofluidic devices varies significantly compared to its microscopic counterpart. The thickness of the electrical double layer (EDL) in these devices spans much of the diameter or channel height leading to the transport of predominantly counterions in the system [8]. The large surface-area-to-volume ratios in these devices have paved the way to several interesting phenomena such as ion permselectivity, rapid mixing, and sample stacking [2,9]. Over the past few years, several numerical and experimental studies on integrated micro and nanofluidic devices have been reported [10–13]. Concentration polarization, a complex phenomenon observed at the junctions of micro-nanofluidic devices, has led to the development of preconcentration devices [14,15] and ion-permselective membranes [16,17]. Wang and Han [18] presented an experimental approach to improve the binding kinetics and the immunoassay detection sensitivity using such interconnect devices. There has also been a growing interest in developing micro/nanofluidic devices as ionic filters and nanofluidic batteries to control both ionic and molecular transport in aqueous solutions [19]. Rubinstein and Shtilman [20] theoretically predicted nonlinear electroosmotic flow (EOF), which is defined as electroosmotic flow of the second-kind at

micro/nanofluidic interfaces and these predictions were later observed by Kim et al. [21] in their experiments. In all of these studies, the transport characteristics are investigated by applying dc electric fields.

Alternating current electroosmosis has also emerged as a predominant technique in driving the fluids in DNA hybridization [7], enhancing species mixing in microfluidic devices [22,23], etc. Ajdari [24] has theoretically predicted unidirectional fluid flow on application of ac electric fields using asymmetric microelectrodes placed on the surface of the microchannel. This was later experimentally observed by Brown et al. [25]. Ramos et al. [26] theoretically analyzed the pumping phenomena using an electroosmotic model. Dutta and Beskok [27] and Erickson and Li [28] presented analytical solutions for ac electroosmotic flows in a 2D straight microchannel. Alternating current electroosmotic flow in curved microchannels was numerically investigated by Chen et al. [29] and showed that the strength of the secondary vortices decreases with an increase in the frequency. Olesen et al. [30] analyzed the nonlinear response of the electrolyte solution under large ac voltages using a simple parallel plate blocking electrode model. Although significant progress has been made in understanding the ac effects in microfluidic devices, few reports are available with regard to the combined effect of the ac and dc electric fields on the nanoscale systems [31]. In this work, an extensive numerical study, based on the continuum theory, is carried out in order to understand the electrokinetic transport and other hydrodynamic effects under the application of combined ac and dc electric fields in micro/nanofluidic interface devices. The simulations are carried out for different EDL thicknesses and nanochannel wall surface charge densities in order to study the flow characteristics. We observe many anomalous and counterintuitive phenomena under a thick EDL regime and at high nanochannel wall surface charge density (in other words, when the nanochannel is highly ion-selective) as the net fluid flow changes from those obtained on the application of only a dc source. These effects are predominantly due to the nonlinear potential distribution along with the presence

¹Corresponding author.

Manuscript received March 22, 2012; final manuscript received July 6, 2012; published online March 19, 2013. Assoc. Editor: Sushanta K. Mitra.

of dual concentration polarization space charges observed near both of the interfaces of the micro/nanochannel at amplitudes greater than the dc voltage and at a low Strouhal number. The large temporal and spatial variations in the polarization space charges near the interfaces lead to finite inertia effects resulting in anomalous changes to the electroosmotic velocity. We calculate the time averaged electroosmotic velocity from the temporal numerical solution and understand its deviation from the dc electroosmotic velocity. Furthermore, we suggest some potential applications using the combined ac/dc electric fields.

The rest of the paper is outlined as follows. Section 2 discusses the theory and the mathematical model, and Sec. 3 describes the canonical micro/nanofluidic interface device with the necessary simulation details. Furthermore, a discussion on the inherent time scales involved in the present study along with the dimensionless governing equations is presented. A detailed discussion of all of the results illustrating the electrokinetic and hydrodynamic effects due to the combined ac/dc electric fields is presented in Sec. 4. Finally, our conclusions are presented in Sec. 5.

2 Theory

2.1 Governing Equations. In this section, the complete set of equations for simulating electrokinetic transport in micro/nanofluidic channels under dc and ac electric fields are presented. Elaborate details and the assumptions underlying these theories can be found in Ref. [5]. In the past, several studies have shown that the continuum theory can accurately describe electrokinetic transport for dimensions larger than several nanometers [10,32,33]. Hence, continuum theory has been used in this paper since the smallest dimension considered in the present study is 30 nm. In electrokinetic flows, the total flux is contributed by three terms: a diffusive component resulting from the concentration gradient, an electrophoretic component arising due to the potential gradient, and a convective component originating from the fluid flow. The total flux of each species in the solution is given by

$$\mathbf{\Gamma}_i = -D_i \nabla c_i - \Omega_i z_i F c_i \nabla \phi + c_i \mathbf{u} \quad (1)$$

where $\mathbf{\Gamma}_i$ is the flux vector, F is Faraday's constant, z_i is the valence, D_i is the diffusion coefficient, Ω_i is the ionic mobility, c_i is the concentration of the i th species, \mathbf{u} is the velocity vector of the fluid flow, and ϕ is the electrical potential. Note that the ionic mobility is related to the diffusion coefficient by Einstein's relation [34] $\Omega_i = D_i/RT$, where R is the ideal gas constant and T is the thermodynamic temperature. The electrical potential distribution is calculated by solving the Poisson equation

$$\nabla \cdot (\epsilon_r \nabla \phi) = -\frac{\rho_e}{\epsilon_0} \quad (2)$$

where ϵ_0 is the permittivity of free space, ϵ_r is the relative permittivity of the medium (here, water is considered as the medium $\epsilon_r = 80$), and ρ_e is the net space charge density of the ions defined as

$$\rho_e = F \left(\sum_{i=1}^m z_i c_i \right) \quad (3)$$

where m is the total number of species considered in the system. The mass transfer of each buffer species is given by the Nernst-Planck equation

$$\frac{\partial c_i}{\partial t} = -\nabla \cdot \mathbf{\Gamma}_i \quad (4)$$

Equations (2), (4), and (1) are the classical Poisson-Nernst-Planck (PNP) equations, which describe the electrochemical

transport. The incompressible Navier-Stokes and the continuity equations are considered, in order to describe the movement of the fluid flow through the channel, i.e.,

$$\rho \left(\frac{\partial \mathbf{u}}{\partial t} + \mathbf{u} \cdot \nabla \mathbf{u} \right) = -\nabla p + \mu \nabla^2 \mathbf{u} + \rho_e \mathbf{E} \quad (5)$$

$$\nabla \cdot \mathbf{u} = 0 \quad (6)$$

where \mathbf{u} is the velocity vector, p is the pressure, ρ and μ are the density and the viscosity of the fluid, respectively, and $\mathbf{E} = -\nabla \phi$ is the electric field. Here, $\rho_e \mathbf{E}$ is the electrostatic body force acting on the fluid due to the space charge density and the applied electric field. The aforementioned set of equations, also referred as the space charge model [35,36], are found to accurately capture the physics observed in the experiments of micro/nanofluidic interface devices [10,12,13,37] and, hence, are used in the present study.

3 Simulation Details and Boundary Conditions

In this study, we considered a rectangular nanochannel of $2 \mu\text{m}$ length (L_0) and 30 nm height (h), connected to two reservoirs ($1 \mu\text{m} \times 1 \mu\text{m}$ cross section) on either side of the channel, as shown in Fig. 1. A 2D simulation study was carried out by assuming that the depth (perpendicular to the plane of the paper) of the micro and nanochannels to be much larger than the length. Reservoir 1 (on the right side), considered as the source, is given a positive voltage (ϕ^{dc}) and reservoir 2, considered as the receiver (on the left), is grounded. An ac voltage is applied after the system reaches a steady-state with the dc field. Both of the reservoirs are filled with a KCl buffer solution with a bulk concentration c_0 . We assume that the concentration of H^+ and OH^- is much lower compared to the bulk concentration of the ionic species and, hence, the water dissociation effects are not considered in the numerical model [10]. We also neglect the Faradaic reactions that occur near the electrode in the present study. The simulation parameters and the boundary conditions are specified as follows. The operating temperature is $T = 300 \text{ K}$ and the density and the viscosity of the fluid are 1000 kg/m^3 and $1.003 \times 10^{-3} \text{ Pa} \cdot \text{s}$, respectively. The diffusivities of K^+ and Cl^- are $1.96 \times 10^{-9} \text{ m}^2/\text{s}$ and $2.03 \times 10^{-9} \text{ m}^2/\text{s}$, respectively. A fixed surface charge density (σ_{ch}) is assumed on the walls of the nanochannel [32]. The boundary conditions at the walls of the nanochannel are

$$\mathbf{n}_w \cdot \nabla \phi = \frac{\sigma_{\text{ch}}}{\epsilon_0 \epsilon_r}, \quad \mathbf{n}_w \cdot \mathbf{\Gamma}_i = 0, \quad \mathbf{u} = 0, \quad \mathbf{n}_w \cdot \nabla p = 0 \quad (7)$$

where \mathbf{n}_w denotes the unit normal vector (pointing outwards) to the nanochannel surface. On the walls of the nanochannel, the fluid velocities are assumed to be subjected to nonslip boundary

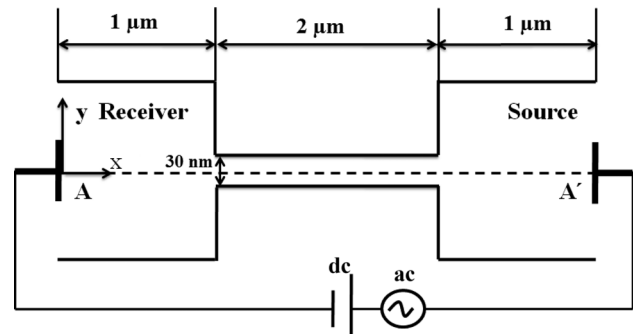


Fig. 1 Simulation setup (not drawn to scale), consisting of a nanochannel of height ($h = 30 \text{ nm}$) connected to two reservoirs of a $1 \mu\text{m} \times 1 \mu\text{m}$ cross section

conditions and the normal flux of each ion is assumed to be zero [38]. Furthermore, several studies in the recent past [14,32,33] have shown that the nanochannel wall surface charge influences the ion-selectivity of the channel and plays a predominant role on the electrokinetic transport. In all of these numerical studies, the charges on the reservoir side walls are assumed to be zero. A similar assumption is made in the present study and the boundary conditions at the walls of the reservoirs are given by

$$\mathbf{n} \cdot \nabla \phi = 0, \quad \mathbf{n} \cdot \boldsymbol{\Gamma}_i = 0, \quad \mathbf{u} = 0, \quad \mathbf{n} \cdot \nabla p = 0 \quad (8)$$

where \mathbf{n} denotes the unit normal vector (pointing outwards) to the reservoir boundary surface in Eq. (8). However, we perform an additional numerical analysis to investigate the effect of the side wall reservoir surface charges on the electrokinetic transport. We briefly discuss these results in Sec. 4.3. Finally, the boundary conditions at the ends of the source (Eq. (9)) and receiver (Eq. (10)) reservoirs are specified as

$$\begin{aligned} \phi &= \phi^{\text{dc}} + \phi^{\text{ac}} \sin(\omega t), \quad c_i = c_0, \quad \mathbf{n} \cdot \nabla \mathbf{u} = 0, \quad p = 0 \quad (9) \\ \phi &= 0, \quad c_i = c_0, \quad \mathbf{n} \cdot \nabla \mathbf{u} = 0, \quad p = 0 \quad (10) \end{aligned}$$

where c_0 is the bulk concentration of the ionic solution, as previously mentioned, ϕ^{dc} is the applied dc voltage, ϕ^{ac} is the amplitude of the ac electric potential, and ω is the angular frequency ($\omega = 2\pi f$, where f is the applied frequency).

We nondimensionalize all of the equations by scaling the distance with the length of the nanochannel (L_0), time with the frequency time scale ($1/f$), concentration with the bulk concentration of the electrolyte solution (c_0), electric potential with $\phi_0 = RT/Fz$, fluid velocity with $U_0 = \epsilon_0 \epsilon_r E_0 \phi_0 / \mu$, where E_0 is the average applied field in the nanochannel (i.e., it is the total voltage drop divided by the nanochannel length), pressure with $p_0 = \mu U_0 / L_0$, and space charge density with $\rho_{e_0} = Fz c_0$. Furthermore, we consider a symmetric monovalent electrolyte ($z_+ = -z_- = z$), such as KCl, in the present analysis. We normalize the diffusion coefficient of each ionic species with the characteristic diffusion coefficient ($D_0 = 2 \times 10^{-9} \text{m}^2/\text{s}$). Applying these scaling variables, the system of governing equations in the dimensionless form can be written as:

- conservation of mass

$$\nabla^* \cdot \mathbf{u}^* = 0 \quad (11)$$

- conservation of momentum

$$\left(\text{St} \frac{\partial \mathbf{u}^*}{\partial t^*} + \mathbf{u}^* \cdot \nabla^* \mathbf{u}^* \right) = \frac{1}{\text{Re}} \left(-\nabla^* p^* + \nabla^{*2} \mathbf{u}^* + \frac{1}{2\beta^2} \rho_e^* \mathbf{E}^* \right) \quad (12)$$

- transport of positive ions

$$\left(\text{St} \frac{\partial c_{\pm}^*}{\partial t^*} + \nabla^* \cdot (c_{\pm}^* \mathbf{u}^*) \right) = \frac{1}{\text{Pe}} (D_{\pm}^* \nabla^{*2} c_{\pm}^* + D_{\pm}^* \nabla^* \cdot (c_{\pm}^* \nabla^* \phi^*)) \quad (13)$$

- transport of negative ions

$$\left(\text{St} \frac{\partial c_{\mp}^*}{\partial t^*} + \nabla^* \cdot (c_{\mp}^* \mathbf{u}^*) \right) = \frac{1}{\text{Pe}} (D_{\mp}^* \nabla^{*2} c_{\mp}^* - D_{\mp}^* \nabla^* \cdot (c_{\mp}^* \nabla^* \phi^*)) \quad (14)$$

- Poisson equation for electrical potential

$$\nabla^{*2} \phi^* = -\frac{1}{2\beta^2} \rho_e^* \quad (15)$$

In the preceding equations, variables with superscript ‘*’ are the dimensionless variables. The various nondimensional numbers are given by $\beta = \lambda_D / L_0$, the Peclet number $\text{Pe} = L_0 U_0 / D_0$, the Reynolds number $\text{Re} = \rho U_0 L_0 / \mu$, and the Strouhal number $\text{St} = f L_0 / U_0$. The Debye length (λ_D), determining the thickness of the EDL, is defined as $\lambda_D = \sqrt{\epsilon_0 \epsilon_r RT / 2F^2 z^2 c_0}$. The inherent time scales present in the system are the viscous time scale (L_0^2 / ν) (where $\nu = \mu / \rho$ is the kinematic viscosity of the fluid), the convective time scale (L_0 / U_0), and the molecular diffusion time scale (L_0^2 / D_0). In the present study, we are interested in understanding the ac effects on the electroosmotic fluid velocity for different EDL thicknesses; hence, the important nondimensional numbers investigated are the Strouhal number (St) and the nondimensional Debye length (β).

The coupled PNP and Navier–Stokes equations are numerically solved using the finite volume method in open field operation and manipulation (OPENFOAM) [39]. The convective terms in the PNP equations are discretized using second-order bounded normalized variation diminishing schemes [40] and all of the Laplacian terms are discretized using a second-order central differencing scheme. The SIMPLE algorithm is used for pressure-velocity coupling [41]. A finer mesh is introduced near the walls; at the entrance and exit of the nanochannel. The model is validated with the numerical results of Daiguji et al. [32,33] and Jin et al. [10]. Along with the numerical validation, the accuracy of the electroosmotic velocity for thin EDL limits is verified with the analytical solution based on the Helmholtz–Smoluchowski equation. These results are not reported here for the sake of brevity (refer to Ref. [42] for details). Furthermore, the results reported here are ensured to be independent of the grid size.

4 Results and Discussion

We initially consider a low bulk ionic concentration $c_0 = 1 \text{mM}$ (corresponding to a thick EDL regime $\beta = 0.0049$) and a nanochannel wall surface charge density, $\sigma_{\text{ch}} = -1 \text{mC/m}^2$ (corresponding to a normalized nanochannel wall surface charge density $\sigma^* = \sigma_{\text{ch}} L_0 / \epsilon_0 \epsilon_r \phi_0 = -109.227$) to investigate the effect of combined ac/dc electric fields on the electrokinetic transport. At this low ionic concentration, the nanochannel is found to behave as an ion-selective membrane leading to the predominant transport of counterions inside the nanochannel. Under these thick EDL limits, we discuss the anomalous electroosmotic transport physics observed inside the nanochannel under different ac/dc electric fields. In order to understand the anomalies and the nonlinear effects in the electrokinetic transport, we calculate the time averaged potential, body force, pressure, and velocity and compare them with the dc case. We note that for a nonlinear system, depending on the degree of nonlinearity, the time averaged quantities under the ac/dc electric field need not be equal to the dc value. Several numerical and experimental studies in the recent past have observed the ion-selectivity of the nanochannel to depend on both the bulk ionic concentration and the nanochannel wall surface charge density [12,13,43]. We extend our study to discuss the influence of the combined ac/dc electric fields on the electrokinetic transport for different dimensionless EDL thicknesses and nanochannel wall surface charge densities.

4.1 Nonlinear Potential Distribution. As previously discussed, the integration of micro/nanofluidic devices leads to many complex phenomena [10,43,44]. The most important phenomenon among them is concentration polarization (CP) [12,17,21], which is predominantly observed in highly ion-selective nanochannels on the application of large dc voltages [16] due to the formation of significant concentration gradients in the electrolyte solution near the interfaces, causing an accumulation of ions on the cathodic side and a depletion of ions on the anodic side for a negatively charged nanochannel surface. At low dc voltages, the electrical potential drop mainly occurs inside the nanochannel since the resistance in the nanochannel is much larger than that in

the reservoirs. The potential drop at such voltages can be assumed to be linear inside the nanochannel. However, at large dc voltages the resistance is very small on the cathodic enrichment side, while the low ionic concentration and the presence of induced polarization space charges at the anodic depletion interface region leads to a large resistance at this region which, in turn, results in a large potential drop near the anodic junction, as shown in the inset of Fig. 2(a). Thus, under large dc electric fields interesting polarization physics is observed near the anodic interface region of the micro/nanochannel and the presence of induced polarization space charges can be understood from the large potential drop developed at this interface region. The polarization effects observed under dc electric fields in ion-selective nanochannels have been extensively studied in the literature [10,37].

We focus our attention in order to investigate the effect of the combined ac and dc electric fields on the electric potential distribution. We note that in the present study, for a typical dc voltage of about 0.5V and a characteristic length scale of about 2 μm, the characteristic velocity is about 4.6 mm/s. For such a system, the convective time scale is approximately 0.44 ms. Furthermore, the kinematic viscosity (ν) of water at 300 K is around

$1.003 \times 10^{-6} \text{m}^2/\text{s}$, resulting in an approximate viscous time scale of 4 μs. These time scales are relevant since we investigate ac electric fields with different frequencies, ranging from 500 Hz – 1 MHz to consider different Strouhal numbers (St). The ac voltages of different amplitudes (ranging from 0.1 – 10V) are considered in order to understand the effect of the ratio $\alpha = \phi^{ac}/\phi^{dc}$ on the nonlinear potential distribution. As expected, under a small ac amplitude ($\alpha = 0.2$), there is no change in the system behavior and the response of the time averaged axial potential distribution is similar to the dc case, as shown in Fig. 2(a). Furthermore, similar physics are observed at all St. The time averaged potential at each position along the centerline of the channel is calculated as

$$\langle \phi^*(x^*) \rangle = \frac{1}{T_p} \int_0^{T_p} \phi^*(x^*) dt \quad (16)$$

It can be shown that, for small α (at any St), the time averaged axial electroosmotic velocity due to the combined ac + dc electric field can be obtained using the principle of linear superposition

$$\langle u_{ac+dc}^* \rangle = u_{dc}^* + \langle u_{ac}^* \rangle \quad (17)$$

where $\langle \rangle = 1/T_p \int_0^{T_p} (\) dt$ is the time averaged component and T_p is the time period of one cycle. The time averaged velocity of the ac component is zero; hence, as expected, the electrokinetic flow is unaffected under small ac perturbations. However, similar to the nonlinear potential distribution observed in micro/nanofluidic channels under a large dc voltage, the application of the combined ac/dc electric fields at amplitudes greater than the dc field (i.e., $\alpha > 1$) and at low St also introduces several changes to the potential distribution, leading to many counterintuitive and anomalous effects in the electrokinetic transport. It is observed that, during the first half of the cycle, the combined high amplitude ac, along with a relatively low dc voltage, causes a large voltage drop (as dc acts in the same direction as the ac voltage) near the anodic interface and no significant voltage drop is observed near the cathodic interface. However, during the other half of the cycle, the combined ac + dc voltage causes a voltage drop near the cathodic interface and no significant voltage drop is observed near the anodic interface. It is important to note that the voltage drop observed near the cathodic interface in this half cycle is relatively smaller (as dc acts against the ac voltage) compared to the voltage drop observed near the anodic interface during the first half of the cycle. Hence, the application of a large ac amplitude at low St, along with a relatively low dc voltage, results in a large voltage drop near the anodic interface and a relatively smaller drop of potential near the cathodic interface. Figures 2(a) and 2(b) show the time averaged nondimensional axial electrical potential distribution for different α and St, respectively. We discuss the frequency effects in detail in a later part of this section.

The regions (with significant voltage drops, as shown in Figs. 2(a) and 2(b)) near both of the interfaces are identified as the concentration polarization space charge regions and the lengths of these polarization charge regions are determined by measuring the large voltage drop regions, as shown schematically in Fig. 3. Thus, we observe dual concentration polarization regions (region I, denoted as CPL-I near the anodic interface and region II, denoted as CPL-II near the cathodic interface) unlike the dc only case where the large voltage drop (for a negatively charged nanochannel) predominantly occurs at the anodic junction due to the polarization space charge regions developed at this junction. Furthermore, the dual polarization lengths are not equal to each other (CPL-I > CPL-II) due to the unequal voltage drops at both of the interfaces. We would also like to point out that the large potential drop occurs from the inner regions of the nanochannel junction and propagates towards the microchannel/reservoir junction, as shown in Figs. 2(a) and 2(b). Thus, the sum of the lengths inside the nanochannel junction and the reservoir junction together constitute

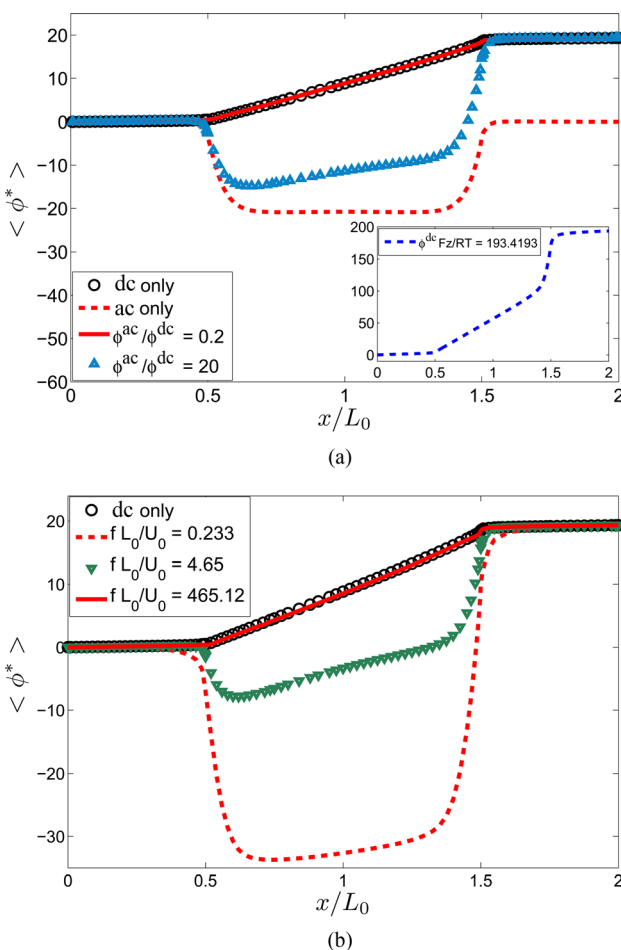


Fig. 2 (a) Numerical results of the time averaged nondimensional axial potential distribution for different $\alpha (= \phi^{ac}/\phi^{dc})$ at a fixed $St = 4.65$. Note: for the ac only case $\phi^{ac} Fz/RT = 386.84$ and $St = 4.65$. The inset of the figure shows the nondimensional axial potential distribution for a large dc voltage $\phi^{dc} Fz/RT = 193.419$. At this voltage, there is a large voltage drop observed at the anodic junction of the micro/nanochannel due to the concentration polarization space charges induced at this junction. **(b)** Variation of the time averaged nondimensional axial potential distribution for different $St (= fL_0/U_0)$ at a fixed $\alpha = 16$. In all of these cases the applied dc voltage is $\phi^{dc} Fz/RT = 19.3419$, $\beta = 0.0049$, and $\sigma^* = -109.227$.

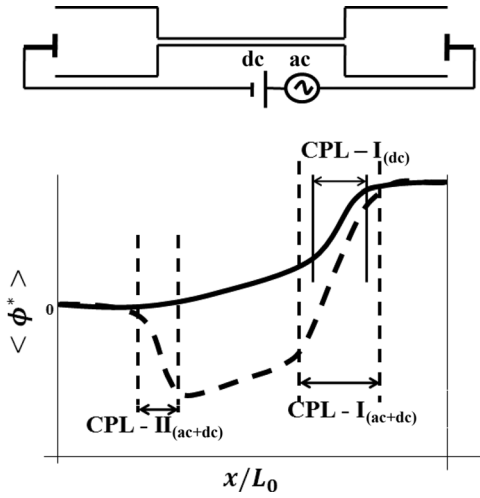


Fig. 3 Schematic of the potential distribution along the length of the micro/nanochannel. The regions with large voltage drops near both the micro/nanofluidic interfaces are defined as concentration polarization regions. Here, CPL-I represents the polarization length at the right end (anodic end) of the nanochannel, while CPL-II indicates the polarization length at the cathodic end. The subscripts dc and ac + dc indicate the lengths when the corresponding fields are applied (the solid line and the dashed line indicate the approximate potential profile for the large dc voltage and large α (and low St) ac + dc field, respectively).

the total CPL length. Similar phenomena of polarization space charge propagation from the inner regions of the nanochannel anodic junction towards the reservoir are observed in the experimental and numerical studies of Mani et al. [12,13] under dc electric fields.

Figure 4(a) shows the normalized CPL as a function of α , at a constant frequency ($St = 4.65$) and dc voltage ($\phi^{dc}Fz/RT = 19.3419$). We discuss two key observations from the figure. First, dual concentration polarization space charge regions are developed at both of the interface regions of the micro/nanochannel when the amplitude of the ac field is greater than the dc field ($\alpha > 1$). Second, it is observed that the polarization lengths developed at both of the interface regions monotonically increase with α . It is important to note that, along with the amplitude, the frequency of the ac field also plays an important role in controlling the polarization space charges at the interfaces. Figure 2(b) shows the time averaged nondimensional axial potential distribution for different St at a constant amplitude ($\alpha = 16$) and dc voltage ($\phi^{dc}Fz/RT = 19.3419$). It can be observed that for low St ($St = 0.233$ and $St = 4.65$) large voltage gradients and dual concentration polarization charge regions are developed at both of the interface regions of micro/nanochannel. However, at large St ($St = 465.12$) or when the frequency time scale is comparable to the viscous time scale (L_0^2/ν), the ac polarization and nonlinear effects decrease and the potential distribution follows the dc case. Figure 4(b) displays the normalized CPL as a function of St in order to further illustrate the aforementioned physics. Thus, under the thick EDL regime, the dual concentration polarization space charge regions (with unequal lengths) are developed at both of the interface regions of a micro/nanofluidic device under low St and for $\alpha > 1$. The same scaling physics is observed even for the case of a higher dc voltage, which is displayed in the inset of Fig. 4(a), where the dual polarization charge regions are built up as $\alpha > 1$. By controlling these polarization lengths we can control the nonlinear effects inside the nanochannel.

4.2 ac Effects on Electrostatic Body Force and Induced Pressure. We discuss the effects of the nonlinear potential distribution and the dual concentration polarization space charge

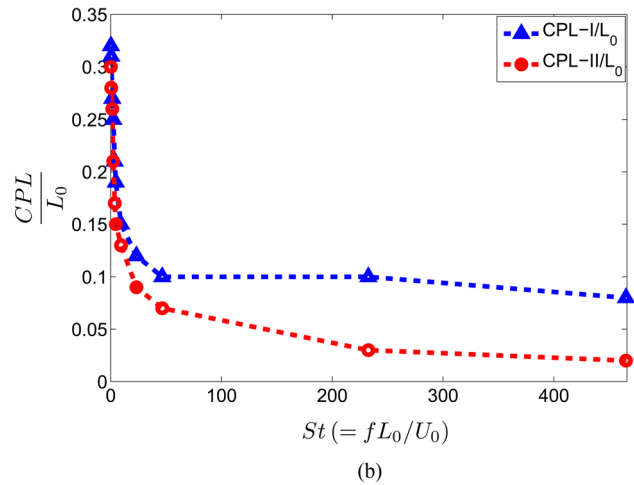
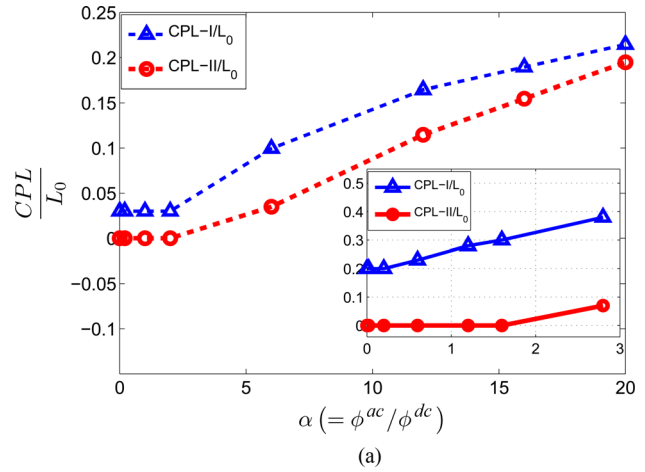


Fig. 4 Normalized dual concentration polarization lengths measured at a fixed $\beta = 0.0049$, $\sigma^* = -109.227$ (a) as a function of α at a fixed $St = 4.65$ and $\phi^{dc}Fz/RT = 19.3419$. The inset of the figure displays the dual concentration polarization lengths for a large dc voltage $\phi^{dc}Fz/RT = 193.419$ (b) as a function of St at a fixed $\alpha = 16$ and $\phi^{dc}Fz/RT = 19.3419$. The resolution of the lengths measured is limited by the grid spacing.

regions on the electrostatic body force and pressure distribution. Figure 5 shows a comparison of the nondimensional axial body force distribution between a low dc field $\phi^{dc}Fz/RT = 19.3419$ and a combined ac/dc electric field with $\alpha = 20$, $St = 4.65$, and

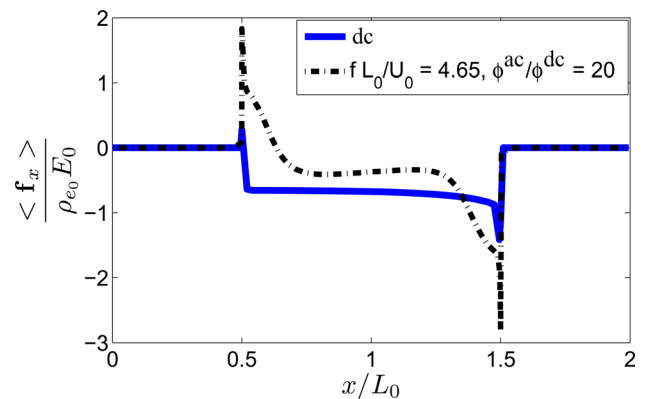


Fig. 5 Nondimensional axial body force distribution (averaged over one time period and averaged across the cross section) for different electric fields at a fixed $\beta = 0.0049$, $\sigma^* = -109.227$, and $\phi^{dc}Fz/RT = 19.3419$

the same dc voltage. For this ac/dc electric field, we observe large body force gradients at both of the interface regions of the micro/nanochannel, compared to the dc case. These observations are primarily due to the large voltage gradients and the polarization space charges observed near both of the interface regions, as discussed in the previous section. The axial body force (\mathbf{f}_x), displayed in Fig. 5, is averaged across the nanochannel and is calculated as

$$\mathbf{f}_x = \frac{1}{h} \int_{-h/2}^{h/2} \rho_e \mathbf{E}_x dy \quad (18)$$

where the subscript x denotes the x -component. The body force is further normalized with the characteristic body force $\rho_{e0} E_0$.

Figure 6(a) displays the time averaged nondimensional axial pressure distribution for different α . To understand the amplitude effects, the frequency ($St = 4.65$) and the dc voltage ($\phi^{dc} Fz/RT = 19.3419$) are kept constant. It can be observed that under small ac perturbations ($\alpha = 0.2$), the time averaged ac/dc axial pressure distribution shows minimal variation compared to that from the dc field, while the application of higher ac amplitudes ($\alpha = 20$) results in large induced pressure gradients at both of the interface regions of the micro/nanochannel due to the large volt-

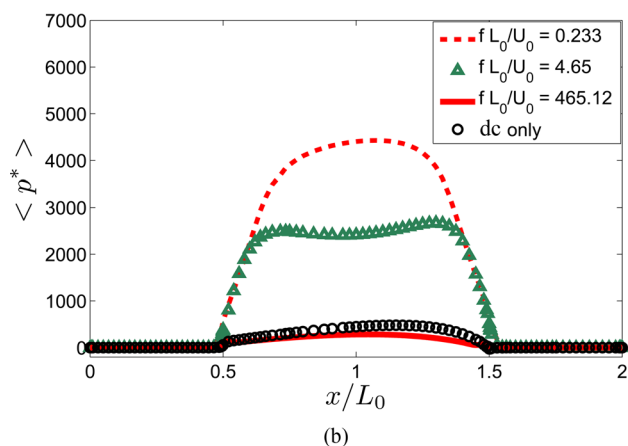
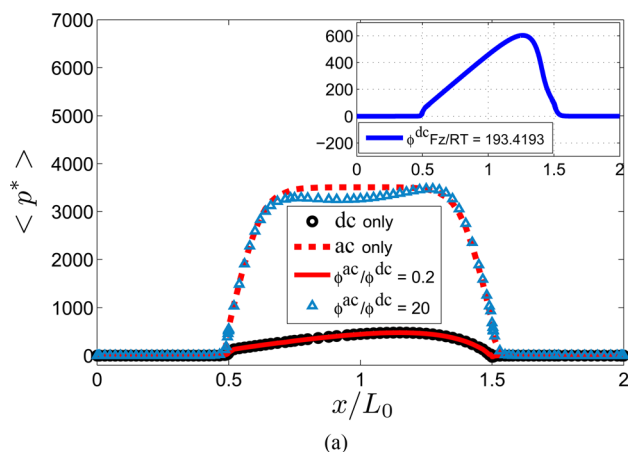


Fig. 6 (a) Time averaged nondimensional axial pressure distribution for different α at a fixed $St = 4.65$. Note: for the ac only case $\phi^{ac} Fz/RT = 386.84$ and $St = 4.65$. The inset of the figure shows the nondimensional axial pressure distribution for a large dc voltage $\phi^{dc} Fz/RT = 193.419$. At this voltage, there is a large induced pressure gradient near the anodic junction of the micro/nanochannel due to the concentration polarization space charges induced at this junction. (b) Variation of the time averaged nondimensional axial pressure distribution for different St at a fixed $\alpha = 16$. In all of these cases $\beta = 0.0049$, $\sigma^* = -109.227$, and $\phi^{dc} Fz/RT = 19.3419$.

age gradients and electrostatic body force observed at these interface regions. Furthermore, this is unlike the physics observed under large dc voltage (see the inset of Fig. 6(a)), where large induced pressure gradients are observed only at the anodic interface region. These results further illustrate the presence of dual polarization space charge regions under combined ac/dc electric fields. Figure 6(b) shows the time averaged nondimensional axial pressure distribution for different St . To study the frequency effects, the amplitude ($\alpha = 16$) and the dc voltage ($\phi^{dc} Fz/RT = 19.3419$) are kept constant. It can be observed that for low St ($St = 0.233$ and $St = 4.65$) large induced pressure gradients are developed at both of the interface regions of the micro/nanochannel. However, at large St ($St = 465.12$) or when the frequency time scale is comparable to the viscous time scale, the nondimensional axial pressure distribution follows the dc case, indicating minimal ac dependence. This can be understood from the fact that the ac polarization effects and voltage gradients also follow the same scaling physics with respect to St , as discussed in the previous section.

In order to understand the effect of voltage gradients and the polarization space charge regions on the electroosmotic velocity inside the nanochannel, we first discuss its effect on the total electrostatic body force acting inside the nanochannel since the electroosmotic velocity is directly dependent on the total electrostatic body force. The total electrostatic body force (\mathbf{F}_x) integrated over the entire channel is calculated as

$$\mathbf{F}_x = \int_{x_s}^{x_s+L_0} h \mathbf{f}_x dx \quad (19)$$

where x_s is the x coordinate where the nanochannel starts, the subscript x denotes the x -coordinate and \mathbf{f}_x is the body force averaged across the nanochannel obtained from Eq. (18).

Figure 7(a) displays the ratio of the total axial electrostatic body force (averaged over one time period and integrated over the entire channel) under the combined ac/dc electric field to the total dc axial electrostatic body force as a function of α at a constant frequency ($St = 4.65$) and dc voltage ($\phi^{dc} Fz/RT = 19.3419$). It is observed that the ratio of the total electrostatic body force acting inside the nanochannel quadratically decreases with respect to α . We understand that the increase in the polarization lengths at the interfaces result in a decrease in the time averaged total ac/dc axial electrostatic body force acting inside the nanochannel. Figure 7(b) shows the ratio of the total axial electrostatic body force (averaged over one time period and integrated over the entire channel) under the combined ac/dc electric field to the total dc axial electrostatic body force as a function of St . To study the frequency effects, the amplitude ($\alpha = 16$) and the dc voltage ($\phi^{dc} Fz/RT = 19.3419$) are kept constant. It can be seen that the time averaged total ac/dc axial electrostatic body force decreases compared to the total dc axial electrostatic body force at low St . However, at large St or when the frequency time scale is comparable to the viscous time scale, the time averaged total ac/dc axial electrostatic body force shows a minimal variation compared to the total dc axial electrostatic body force. Again, these results can be understood from the fact that the dual concentration polarization space charges and strong voltage gradients at both of the interfaces are observed at low St . However, at large St , the ac polarization effects are minimal, as elaborately discussed in the previous section.

4.3 Electroosmotic Flow. With the understanding of the effect of the combined ac/dc electric fields on the total electrostatic body force, we investigate the effect of these electric fields on the axial electroosmotic flow (EOF) velocity inside the nanochannel. Figure 8(a) shows the ratio of the time averaged ac/dc axial electroosmotic velocity to the dc axial electroosmotic velocity as a function of α . To understand the amplitude effects, the frequency ($St = 4.65$) and dc voltage ($\phi^{dc} Fz/RT = 19.3419$) are

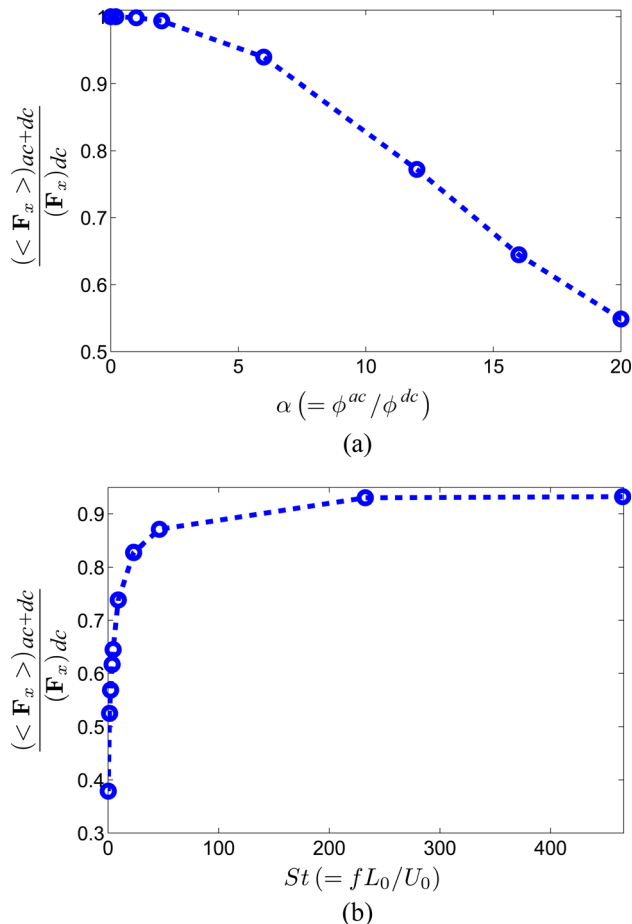


Fig. 7 The ratio of the total axial electrostatic body force (averaged over one time period) integrated over the entire channel under the combined ac/dc electric field to the total dc axial electrostatic body force for a fixed $\beta = 0.0049$, $\sigma^* = -109.227$, and $\phi^{dc}Fz/RT = 19.3419$ (a) as a function of α at a fixed $St = 4.65$, and (b) as a function of St at a fixed $\alpha = 16$

kept constant and the electroosmotic velocity is evaluated at the midpoint of the nanochannel. It is observed that the ratio of the time averaged ac/dc axial electroosmotic velocity inside the nanochannel quadratically decreases with respect to α . This can be understood from the fact that the ratio of the time averaged total ac/dc axial electrostatic body force to the total dc axial electrostatic body force exhibits a similar scaling relation with respect to α and the underlying physics is already discussed in an earlier section. The inset of Fig. 8(a) also reveals similar scaling physics with respect to α under a higher dc voltage ($\phi^{dc}Fz/RT = 193.419$). The deviation of the time averaged ac/dc velocities from the dc velocity illustrates the strong nonlinearities present in the system. Figure 8(b) displays the time averaged nondimensional axial electroosmotic velocity across the cross section of the nanochannel for different α in order to further illustrate the decrease in the time averaged axial electroosmotic velocity under large α ($\alpha = 20$). However, minimal variations in the time averaged axial electroosmotic velocity compared to the dc velocity are observed under small amplitude perturbations ($\alpha = 0.2$). Figure 9(a) shows the ratio of the time averaged ac/dc axial electroosmotic velocity to the dc axial electroosmotic velocity as a function of St at a constant amplitude ($\alpha = 16$) and dc voltage ($\phi^{dc}Fz/RT = 19.3419$). The electroosmotic velocity is evaluated at the midpoint of the nanochannel. It can be seen that the time averaged ac/dc axial electroosmotic velocity decreases compared to the dc axial electroosmotic velocity at low St . However, at large St or when the frequency time scale is comparable to the viscous

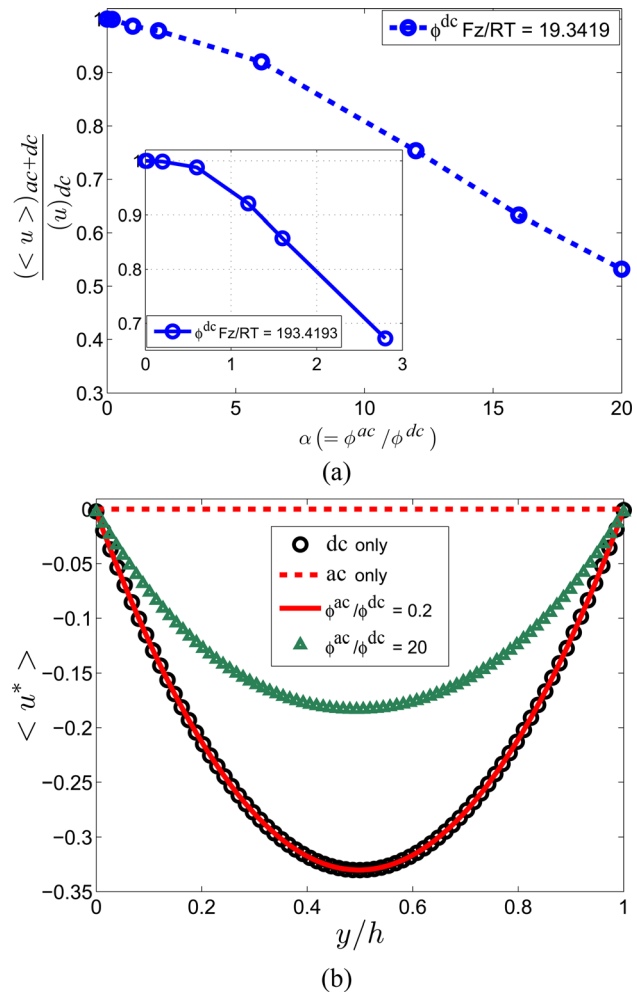


Fig. 8 Numerically calculated velocities (averaged over one time period) measured at the center of the nanochannel ($x/L_0 = 1$) at a fixed $St = 4.65$, $\beta = 0.0049$, $\sigma^* = -109.227$, and $\phi^{dc}Fz/RT = 19.3419$. (a) The ratio of the time averaged ac/dc axial electroosmotic velocity to the dc axial electroosmotic velocity as a function of α . The inset of the figure displays the velocity variation with α for a large dc voltage $\phi^{dc}Fz/RT = 193.419$. (b) The variation of the time averaged nondimensional axial electroosmotic velocity across the cross section of the nanochannel for different α . For the ac only case $\phi^{ac}Fz/RT = 386.84$ and $St = 4.65$. Note: the negative sign indicates the flow direction from right to left.

time scale, the time averaged ac/dc axial electroosmotic velocity shows minimal variation compared to the dc axial electroosmotic velocity. These results, again, can be understood from the fact that the ratio of the time averaged total ac/dc axial electrostatic body force to the total dc axial electrostatic body force exhibits a similar behavior with respect to St and the reason for this variation is discussed in an earlier section. Figure 9(b) displays the time averaged nondimensional axial electroosmotic velocity across the cross section of the nanochannel for different St ($St = 0.233$, 4.65, and 465.12) in order to further illustrate the aforementioned physics.

Finally, we would also like to briefly point out that, with an application of the ac field alone, we observe a symmetric voltage drop and induced pressure gradients at both of the interfaces of the micro/nanochannel (see Figs. 2(a) and 6(a)). Due to this symmetry, it can be observed from Fig. 8(b) that the time averaged axial velocity across the nanochannel is zero and, as expected, there is no net fluid flow inside the nanochannel.

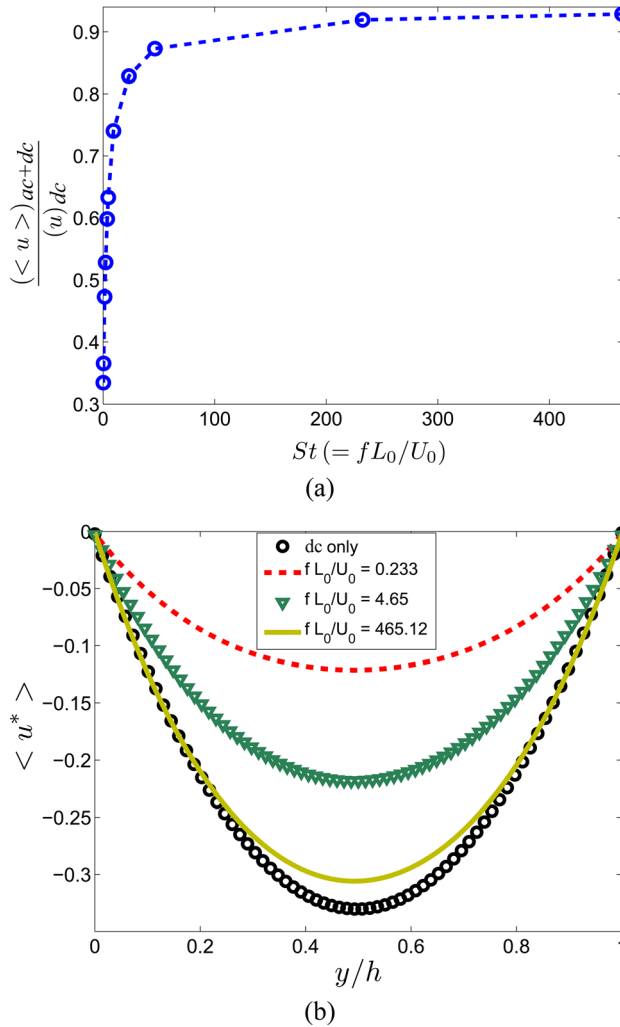


Fig. 9 Numerically calculated velocities (averaged over one time period) measured at the center of the nanochannel ($x/L_0 = 1$) at a fixed $\alpha = 16$, $\beta = 0.0049$, $\sigma^* = -109.227$, and $\phi^{dc}Fz/RT = 19.3419$. (a) The ratio of the time averaged ac/dc axial electroosmotic velocity to the dc axial electroosmotic velocity as a function of St . (b) The variation of the time averaged nondimensional axial electroosmotic velocity across the cross section of the nanochannel for different St .

In all of the aforementioned results, in order to understand the effect of the combined ac/dc electric fields on the electrokinetic transport under thick EDL regimes, a low ionic concentration of about 1 mM was considered. Under the thick electrical double layer regime the nanochannel behaves as an ion-selective membrane, i.e., there is a predominant transport of counterions inside the nanochannel. Along with the bulk ionic concentration, the nanochannel wall surface charge density also controls the ion-selectivity of the nanochannel [12,13,43]. We extend our study and provide additional numerical results to explain the effect of the combined ac/dc electric fields on the electrokinetic transport for different system parameters using the dimensionless electrical double layer thickness ($\beta = \lambda_D/L_0$) and the normalized wall surface charge density of the nanochannel (σ^*). Figure 10 displays the ratio of the time averaged ac/dc axial electroosmotic velocity to the dc axial electroosmotic velocity as a function of St for different nondimensional EDL thicknesses (β). Here, β is varied by changing the bulk ionic concentration (c_0) of the electrolyte. To understand the frequency effects, the amplitude ($\alpha = 6$) and the dc voltage ($\phi^{dc}Fz/RT = 19.3419$) are kept constant and the velocities are evaluated at the midpoint of the nanochannel. It is

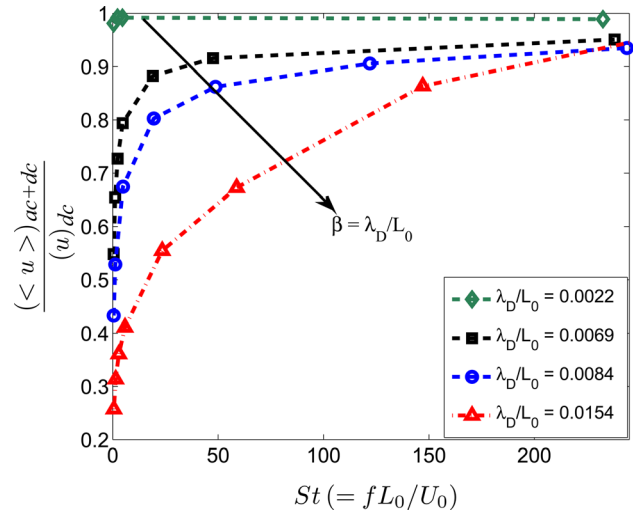


Fig. 10 Effect of the dimensionless EDL thickness ($\beta = \lambda_D/L_0$) and St on the ratio of the time averaged ac/dc axial electroosmotic velocity to the dc axial electroosmotic velocity. The velocity is measured at the center of the nanochannel ($x/L_0 = 1$) at a fixed $\alpha = 6$, $\sigma^* = -109.227$, and $\phi^{dc}Fz/RT = 19.3419$. Here, β is varied by changing the bulk ionic concentration (c_0) of the electrolyte.

observed that the voltage gradients and the dual concentration polarization space charge regions (near both of the interfaces of the micro/nanochannel) predominantly observed at a low St increase as the EDL thickness increases, resulting in a significant decrease in the time averaged ac/dc axial electroosmotic velocity compared to the dc axial electroosmotic velocity. However, when the concentration of the electrolyte increases, i.e., as the nondimensional EDL thickness (β) reduces and the ion-selectivity of the nanochannel decreases, the polarization and nonlinear effects under the combined ac/dc electric fields decrease and the time averaged ac/dc axial electroosmotic velocity approaches the dc axial electroosmotic velocity, indicating minimal ac dependence on the electrokinetic transport.

Figure 11 shows the ratio of the time averaged ac/dc axial electroosmotic velocity to the dc axial electroosmotic velocity as a function of St for different normalized nanochannel wall surface

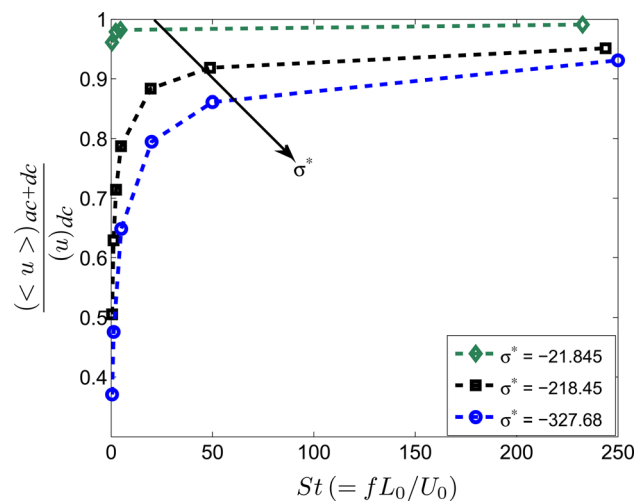


Fig. 11 Effect of the normalized surface charge density (σ^*) and St on the ratio of the time averaged ac/dc axial electroosmotic velocity to the dc axial electroosmotic velocity. The velocity is measured at the center of the nanochannel ($x/L_0 = 1$) at a fixed $\alpha = 6$, $\beta = 0.0049$, and $\phi^{dc}Fz/RT = 19.3419$.

charge densities (σ^*). Here, the amplitude ($\alpha = 6$) and the dc voltage ($\phi^{dc}Fz/RT = 19.3419$) are kept constant. It is observed that at a large nanochannel wall surface charge density, the channel essentially behaves as an ion-selective membrane. As expected, a higher ion-selectivity of the nanochannel leads to stronger polarization and nonlinear effects at low St, resulting in a significant decrease in the time averaged ac/dc axial electroosmotic velocity compared to the dc axial electroosmotic velocity. Furthermore, the results are consistent with our previous arguments that the ac fields have a minimal dependence on the electrokinetic transport as the ion-selectivity of the nanochannel decreases, which is achieved in this case by reducing the nanochannel wall surface charge density (σ^*). We would also like to highlight that the scaling physics, with respect to α , is consistent with our previous observations for cases of higher EDL thickness and larger σ^* . From the aforementioned results, we conclude that the ion-selectivity of the nanochannel plays an important role in controlling the concentration polarization effects and electrokinetic transport in micro/nanofluidic interface devices under combined ac/dc electric fields.

As discussed earlier, we perform an additional numerical analysis in order to investigate the effect of the side wall reservoir surface charges (σ_w) on the electrokinetic transport under the combined ac/dc electric fields. The tests are carried out for different reservoir side wall surface charge densities, i.e., σ_w/σ_{ch} ranges from -2 to 2 at a constant nanochannel wall surface charge density $\sigma^* = -109.227$ and $\beta = 0.0049$. The amplitude ($\alpha = 6$), frequency (St = 4.65), and dc voltage ($\phi^{dc}Fz/RT = 19.3419$) are also kept constant. As expected, it is observed that the introduction of a heterogeneous surface charge at the channel entrance (i.e., if the surface charge polarity on the nanochannel walls (σ_{ch}) is opposite to the reservoir side walls (σ_w)) leads to larger voltage gradients and higher polarization effects at both of the interfaces compared to the homogeneous system under the same ac fields. These polarization effects, in turn, result in a further decrease in the time averaged ac/dc axial electroosmotic velocity inside the nanochannel. For instance, we observe about a 10% decrease in the time averaged axial electroosmotic velocity under the same ac/dc electric field for a heterogeneous case ($\sigma_w/\sigma_{ch} = -2$) compared to the neutral side wall case. Although the heterogeneous surface charge distribution at the channel entrance leads to additional polarization effects, we understand that the nanochannel wall surface charge density and the ionic concentration of the electrolyte (i.e., the ion-selectivity of the nanochannel) play a more important role in controlling the concentration polarization effects and electrokinetic transport in micro/nanofluidic interface devices under combined ac/dc electric fields. Furthermore, we would like to point out that all of the aforementioned physics can also be observed for larger reservoir dimensions, when the system is perturbed under a low Strouhal number. To our knowledge, the nonlinear effects due to the combined ac/dc electric fields in highly ion-selective nanofluidic devices and the presence of dual concentration polarization regions at both of the interfaces of the micro/nanofluidic device have not been reported before in the literature and by controlling these lengths, we can control the nonlinear effects and also modulate the fluid flow.

With the understanding of nonlinear electrokinetic transport physics under combined ac/dc electric fields in highly ion-selective nanochannels, we suggest some potential applications of these electric fields. The large voltage gradients (inducing large resistances) developed near both of the interfaces of the micro/nanochannel under low St and at large α can be used to preconcentrate proteins and biological species to improve its detection. The large electric fields due to the presence of concentration polarization space charges at both of the interfaces, along with the large induced pressure gradients at the interfaces, lead to electrokinetic vortices at both of these interface regions, which can provide multiple mixing regions. This is unlike the electrokinetic vortices observed only at the anodic depletion interface region under the application of large dc electric fields. Adequate mixing ratios can

be achieved by controlling the frequency and amplitude of the ac fields. Furthermore, by controlling the electroosmotic transport inside the nanochannel using the combined ac + dc electric fields, these fields can be potentially used in reaction kinetics to enhance the reaction rates [45] inside the nanochannel. Thus, along with offering interesting physics at the interface regions, the application of combined ac and dc electric fields also paves way for many potential applications in micro/nanofluidic interconnect devices.

5 Conclusions

In this work, the effect of the combined ac and dc electric fields on the electrokinetic transport and other hydrodynamic properties are investigated in micro/nanofluidic interface devices. Many anomalous and counterintuitive observations on the electrokinetic transport under different ac/dc electric fields and the underlying physics behind these observations are discussed. For a highly ion-selective nanochannel, strong nonlinear potential distribution and dual concentration polarization space charges at both of the interface regions of the micro/nanochannel are observed at ac amplitudes greater than the dc field and at low St. The large voltage gradients and the polarization space charges developed near both of the interfaces result in significant changes in the electrostatic body force and in the electroosmotic velocity compared to the dc case. The ion-selectivity of the nanochannel is found to play an important role in controlling the concentration polarization effects and electrokinetic transport in micro/nanofluidic interface devices under combined ac/dc electric fields. We believe that the understanding of the nonlinear transport physics at these interfaces can lead to novel designs of micro/nanofluidic interconnect devices and we suggest some potential applications utilizing the ac/dc electric fields.

Acknowledgment

This work was supported by the NSF under Grant No. 0120978 (Water CAMPWS, UIUC), Grant No. 0328162 (nano-CEMMS, UIUC), and Grant Nos. 0810294, 0852657, and 0915718. The authors would like to thank Dr. Xiaozhong Jin for helpful discussions.

Nomenclature

c = concentration (mM)
 D = diffusion coefficient (m^2/s)
 E = electric field (V/m)
 f = frequency (Hz)
 f_x = axial body force averaged across nanochannel (N/m^3)
 F = Faraday constant (C/mol)
 F_x = total axial electrostatic force per unit width (N/m)
 h = nanochannel height (m)
 L_0 = nanochannel length (m)
 m = number of species
 \mathbf{n} = unit normal vector
 p = pressure of the fluid (N/m^2)
 Pe = Peclet number
 R = ideal gas constant (J/molK)
 Re = Reynolds number
 St = Strouhal number
 T = thermodynamic temperature (K)
 t = time (s)
 T_p = time period (s)
 \mathbf{u} = velocity vector (m/s)
 x = axial direction
 y = lateral direction
 z = valence

Greek Symbols

α = ratio of ac amplitude to dc potential
 β = dimensionless Debye length

Γ = flux vector (mol/m²s)
 ϵ_0 = permittivity of free space
 ϵ_r = relative permittivity of medium
 λ_D = Debye length (m)
 μ = viscosity of fluid (Pa · s)
 ν = kinematic viscosity of fluid (m²/s)
 ρ = density of fluid (kg/m³)
 ρ_e = space charge density (C/m³)
 σ = surface charge density (C/m²)
 ϕ = electrical potential (V)
 ω = angular frequency (rad/s)
 Ω = mobility (m²/mol/Js)

Subscripts

ch = nanochannel
 i = i th species
 w = wall
 0 = bulk/characteristic variable
 + = positive monovalence
 – = negative monovalence

Superscripts

ac = ac component
 dc = dc component
 * = dimensionless variable

References

- Hong, J. W., and Quake, S. R., 2003, "Integrated Nanoliter Systems," *Nat. Biotechnol.*, **21**, pp. 1179–1183.
- Prakash, S., Piruska, A., Gatimu, E. N., Bohn, P. W., Sweedler, J. V., and Shannon, M. A., 2008, "Nanofluidics: Systems and Applications," *IEEE Sens. J.*, **8**(5), pp. 441–450.
- Schoch, R. B., Han, J., and Renaud, P., 2008, "Transport Phenomena in Nanofluidics," *Rev. Mod. Phys.*, **80**, pp. 839–883.
- Chang, H.-C., and Yossifon, G., 2009, "Understanding Electrokinetics at the Nanoscale: A Perspective," *Biomicrofluidics*, **3**, p. 012001.
- Karniadakis, G. E., Beskok, A., and Aluru, N. R., 2005, *Microflows and Nanoflows: Fundamentals and Simulation*, Springer, New York.
- Bayraktar, T., and Pidugu, S. B., 2006, "Characterization of Liquid Flows in Microfluidic System," *Int. J. Heat Mass Transfer*, **49**, pp. 815–824.
- Wong, P. K., Chen, C.-Y., Wang, T.-H., and Ho, C.-M., 2004, "Electrokinetic Bioprocessor for Concentrating Cells and Molecules," *Anal. Chem.*, **76**, pp. 6908–6914.
- Qiao, R., and Aluru, N. R., 2003, "Ion Concentrations and Velocity Profiles in Nanochannel Electroosmotic Flows," *J. Chem. Phys.*, **118**, pp. 4692–4701.
- Kuo, T.-C., Cannon, D. M., Jr., Shannon, M. A., Bohn, P. W., and Sweedler, J. V., 2003, "Hybrid Three-Dimensional Nanofluidic/Microfluidic Devices Using Molecular Gates," *Sens. Actuators, A*, **102**, pp. 223–233.
- Jin, X., Joseph, S., Gatimu, E. N., Bohn, P. W., and Aluru, N. R., 2007, "Induced Electrokinetic Transport in Micro-Nanofluidic Interconnect Devices," *Langmuir*, **23**, pp. 13209–13222.
- Gatimu, E. N., Jin, X., Aluru, N. R., and Bohn, P. W., 2008, "Perturbation of Microfluidic Transport Following Electrokinetic Injection Through a Nanocapillary Array Membrane: Injection and Biphasic Recovery," *J. Phys. Chem. C*, **112**, pp. 19242–19247.
- Mani, A., Zangle, T. A., and Santiago, J. G., 2009, "On the Propagation of Concentration Polarization From Microchannel-Nanochannel Interfaces. Part I. Analytical Model and Characteristic Analysis," *Langmuir*, **25**, pp. 3898–3908.
- Zangle, T. A., Mani, A., and Santiago, J. G., 2009, "On the Propagation of Concentration Polarization From Microchannel-Nanochannel Interfaces. Part II. Numerical and Experimental Study," *Langmuir*, **25**, pp. 3909–3916.
- Wang, Y., Pant, K., Chen, Z., Wang, G., Diffey, W. F., Ashley, P., and Sundaram, S., 2009, "Numerical Analysis of Electrokinetic Transport in Micro-Nanofluidic Interconnect Preconcentrator in Hydrodynamic Flow," *Microfluid. Nanofluid.*, **7**, pp. 683–696.
- Hatch, A. V., Herr, A. E., Throckmorton, D. J., Brennan, J. S., and Singh, A. K., 2006, "Integrated Preconcentration SDS-PAGE of Proteins in Microchips Using Photopatterned Cross-Linked Polyacrylamide Gels," *Anal. Chem.*, **78**, pp. 4976–4984.
- Yossifon, G., and Chang, H.-C., 2008, "Selection of Nonequilibrium Overlimiting Currents: Universal Depletion Layer Formation Dynamics and Vortex Instability," *Phys. Rev. Lett.*, **101**, p. 254501.
- Dukhin, S. S., and Shilov, V. N., 1969, "Theory of Static Polarization of the Diffuse Part of the Thin Electric Double Layer of Spherical Particles," *Kolloid. Zh.*, **31**, pp. 706–713.
- Wang, Y. C., and Han, J., 2008, "Pre-Binding Dynamic Range and Sensitivity Enhancement for Immuno-Sensors Using Nanofluidic Preconcentrator," *Lab Chip*, **8**, pp. 392–394.
- Vlassiuk, I., Smirnov, S., and Siwy, Z., 2008, "Ionic Selectivity of Single Nanochannels," *Nano Lett.*, **8**, pp. 1978–1985.
- Rubinstein, I., and Shilman, L., 1979, "Voltage Against Current Curves of Cation Exchange Membranes," *J. Chem. Soc., Faraday Trans. 2*, **75**, pp. 231–246.
- Kim, S. J., Wang, Y.-C., Lee, J. H., Jang, H., and Han, J., 2007, "Concentration Polarization and Nonlinear Electrokinetic Flow Near a Nanofluidic Channel," *Phys. Rev. Lett.*, **99**, p. 044501.
- Oddy, M. H., Santiago, J. G., and Mikkelsen, J. C., 2001, "Electrokinetic Instability Micromixing," *Anal. Chem.*, **73**, pp. 5822–5832.
- Tang, G. H., Li, Z., Wang, J. K., He, Y. L., and Tao, W. Q., 2006, "Electroosmotic Flow and Mixing in Microchannels With the Lattice Boltzmann Method," *J. Appl. Phys.*, **100**, p. 094908.
- Ajdari, A., 2000, "Pumping Liquids Using Asymmetric Electrode Arrays," *Phys. Rev. E*, **61**, pp. R45–R48.
- Brown, A. B. D., Smith, C. G., and Rennie, A. R., 2001, "Pumping of Water With AC Electric Fields Applied to Asymmetric Pairs of Microelectrodes," *Phys. Rev. E*, **63**, p. 016305.
- Ramos, A., González, A., Castellanos, A., Green, N. G., and Morgan, H., 2003, "Pumping of Liquids With AC Voltages Applied to Asymmetric Pairs of Microelectrodes," *Phys. Rev. E*, **67**, p. 056302.
- Dutta, P., and Beskok, A., 2001, "Analytical Solution of Time Periodic Electroosmotic Flows: Analogies to Stokes' Second Problem," *Anal. Chem.*, **73**, pp. 5097–5102.
- Erickson, D., and Li, D., 2003, "Analysis of Alternating Current Electroosmotic Flows in a Rectangular Microchannel," *Langmuir*, **19**, pp. 5421–5430.
- Chen, J. K., Luo, W. J., and Yang, R. J., 2006, "Electroosmotic Flow Driven by DC and AC Electric Fields in Curved Microchannels," *Jpn. J. Appl. Phys.*, **45**, pp. 7983–7990.
- Olesen, L. H., Bazant, M. Z., and Bruus, H., 2010, "Strongly Nonlinear Dynamics of Electrolytes Under Large AC Voltages," *Phys. Rev. E*, **82**, p. 011501.
- Bhattacharyya, S., and Nayak, A. K., 2008, "Time Periodic Electro-Osmotic Transport in a Charged Micro/Nanochannel," *Colloid. Surf. A*, **325**, pp. 152–159.
- Daiguji, H., Yang, P., and Majumdar, A., 2004, "Ion Transport in Nanofluidic Channels," *Nano Lett.*, **4**, pp. 137–142.
- Daiguji, H., Yang, P., Szeri, A. J., and Majumdar, A., 2004, "Electrochemomechanical Energy Conversion in Nanofluidic Channels," *Nano Lett.*, **4**, pp. 2315–2321.
- Probstein, R. F., 1994, *Physicochemical Hydrodynamics: An Introduction*, John Wiley and Sons, New York.
- Gross, R., and Osterle, J., 1968, "Membrane Transport Characteristics of Ultra-fine Capillaries," *J. Chem. Phys.*, **49**, pp. 228–234.
- Wang, X.-L., Tsuru, T., Nakao, S.-I., and Kimura, S., 1995, "Electrolyte Transport Through Nanofiltration Membranes by the Space-Charge Model and the Comparison With Teorell-Meyer-Sievers Model," *J. Membr. Sci.*, **103**, pp. 117–133.
- Yossifon, G., Mushenheim, P., Chang, Y. C., and Chang, H.-C., 2009, "Nonlinear Current-Voltage Characteristics of Nano-Channels," *Phys. Rev. E*, **79**, p. 046305.
- Chang, C. C., and Yang, R. J., 2010, "Electrokinetic Energy Conversion in Micrometer-Length Nanofluidic Channels," *Microfluid. Nanofluid.*, **9**, pp. 225–241.
- OpenCFD Ltd., "The Open Source CFD Toolbox," <http://www.openfoam.com/>
- Toro, E. F., 1999, *Riemann Solvers and Numerical Methods for Fluid Dynamics*, Springer-Verlag, Berlin.
- Versteeg, H. K., and Malalasekera, W., 2007, *An Introduction to Computational Fluid Dynamics: The Finite Volume Method*, 2nd ed., Pearson Education Ltd., Essex.
- Nandigana, V. V. R., 2011, "Nonlinear Electrokinetic Transport and Its Applications Under Combined AC and DC Fields in Micro/Nanofluidic Interface Devices," M.S. thesis, University of Illinois at Urbana-Champaign, Urbana, IL.
- Schoch, R. B., van Lintel, H., and Renaud, P., 2005, "Effect of the Surface Charge on Ion Transport Through Nanoslits," *Phys. Fluids*, **17**, p. 100604.
- Wang, Y.-C., Stevens, A. L., and Han, J., 2005, "Million-Fold Preconcentration of Proteins and Peptides by Nanofluidic Filter," *Anal. Chem.*, **77**, pp. 4293–4299.
- Nandigana, V. V. R., and Aluru, N. R., 2010, "Reaction Kinetics in Micro/Nanofluidic Devices: Effect of Confinement and AC Voltage," 63rd Annual Meeting of the APS Division of Fluid Dynamics, Long Beach, CA, Nov. 21–23, Vol. 55, Abstract ID No. BAPS.2010.DFD.HP.3, <http://meetings.aps.org/link/BAPS.2010.DFD.HP.3>